

Critical thermalization of a disordered dipolar spin system in diamond

G. Kucsko,^{1†} S. Choi,^{1†} J. Choi,^{1,2†} P. C. Maurer,³ H. Sumiya,⁴ S. Onoda,⁵
J. Isoya,⁶ F. Jelezko,⁷ E. Demler,¹ N. Y. Yao,⁸ M. D. Lukin^{1*}

¹Department of Physics, Harvard University,
Cambridge, MA 02138, USA

²John A. Paulson School of Engineering and Applied Sciences, Harvard University,
Cambridge, MA 02138, USA

³Department of Physics, Stanford University,
Stanford, California 94305, USA

⁴Sumitomo Electric Industries Ltd., Itami, Hyougo, 664-0016, Japan

⁵Takasaki Advanced Radiation Research Institute,
National Institutes for Quantum and Radiological Science and Technology,
1233 Watanuki, Takasaki, Gunma 370-1292, Japan

⁶Research Centre for Knowledge Communities
University of Tsukuba, Tsukuba, Ibaraki 305-8550, Japan

⁷Institut für Quantenoptik, Universität Ulm,
89081 Ulm, Germany

⁸Department of Physics, University of California Berkeley,
Berkeley, California 94720, USA

[†]These authors contributed equally to this work.

^{*}To whom correspondence should be addressed
E-mail: lukin@physics.harvard.edu.

Statistical mechanics underlies our understanding of macroscopic quantum systems. It is based on the assumption that out-of-equilibrium systems rapidly

approach their equilibrium states, forgetting any information about their microscopic initial conditions. This fundamental paradigm is challenged by disordered systems, in which a slowdown or even absence of thermalization is expected. We report the observation of critical thermalization in a three dimensional ensemble of $\sim 10^6$ electronic spins coupled via dipolar interactions. By controlling the spin states of nitrogen vacancy color centers in diamond, we observe slow, sub-exponential relaxation dynamics consistent with power laws that exhibit disorder-dependent exponents; this behavior is modified at late times owing to many-body interactions. These observations are quantitatively explained by a resonance counting theory that incorporates the effects of both disorder and interactions.

Nearly six decades ago, Anderson predicted that the interplay between long-range couplings and disorder in quantum systems can lead to a novel regime of slow, sub-diffusive thermalization (1). This is in stark contrast to both conventional ergodic systems and disordered systems with short-range hopping, where disorder can arrest dynamics, resulting in the breakdown of ergodicity. Termed Anderson localization, the latter effect has been observed in systems ranging from acoustic and optical waves to cold atomic gases (2–5); more recently, it has been shown that localization can persist even in strongly-interacting, isolated quantum systems, a phenomenon dubbed many-body localization (6–11). The addition of long-range couplings tends to facilitate delocalization, leading to a regime where ergodicity and localization compete (12). This so-called critical regime is realized by dipolar spins in 3D, where a combination of power-law interactions, dimensionality, and disorder govern the microscopic dynamics. Such criticality has been extensively explored in theory, but, as yet, not observed in experiment (1, 13–15). In particular, the role of interactions in such systems is not fully understood; indeed, strong interactions can play two contrasting roles, either strengthening the effective

disorder (9) or facilitating thermalization via many-body resonances (12, 16).

Our approach to the realization and study of critical dynamics makes use of disordered, strongly interacting spin impurities associated with Nitrogen Vacancy (NV) centers in diamond. In particular, we study cross-relaxation between two independently addressable and oppositely polarized electronic spin ensembles (Fig. 1A). We directly probe the spin decay dynamics as a function of disorder and identify a regime of critical slow relaxation. Our experimental system consists of a dense ensemble of NV centers under ambient conditions. The sample was prepared via electron irradiation of a type Ib diamond, yielding a high conversion efficiency from nitrogen to NV (17). A diamond nanobeam (~ 300 nm \times 300 nm \times 20 μ m) is fabricated via reactive ion etching in order to precisely control excitation spot size and to reduce microwave field inhomogeneity (17, 18). In our experiments, a laser beam is focused onto a diffraction limited spot (~ 200 nm) at the center of the beam, realizing an effective 3D system (Fig. 1B). Each NV center constitutes a $S = 1$ electronic spin, which can be initialized, manipulated and optically read out. The spin projections $|m_s = \pm 1\rangle$, are separated from $|m_s = 0\rangle$ by a crystal field splitting, $\Delta_0 = (2\pi) 2.87$ GHz. An external magnetic field, B_{\parallel} , along the NV axis can further split the $|m_s = \pm 1\rangle$ states, isolating an effective two-level systems $|m_s = 0\rangle$ and $|m_s = -1\rangle$ with transition frequency ω_0 and Pauli spin operators $\vec{\sigma}$ (Fig. 1E). The NV concentration in our sample is approximately 45 ppm (17), yielding an average NV-to-NV separation of 5 nm and a corresponding typical dipolar interaction strength $J \sim (2\pi) 420$ kHz; crucially, this is significantly faster than typical spin coherence times (19). Owing to lattice strain and an abundance of other paramagnetic impurities (consisting mainly of P1 centers and ^{13}C nuclear spins), our system is also characterized by strong disorder; for each NV, this disorder arises from effective random fields generated by its local environment. The magnitude of the disorder W can be directly extracted from an electron spin resonance (ESR) measurement (Fig. 1D), yielding a Gaussian distribution with a standard deviation $W \approx (2\pi) 4.0$ MHz (17).

Each NV center in the ensemble can be oriented along any of the four crystallographic axes of the diamond lattice. Different projections of an external magnetic field naturally lead to distinct energy splittings and define four unique NV groups, $\{A, B, C, D\}$, which can be individually addressed and controlled in a finite B-field via resonant microwave radiation (Fig. 1E). By tuning the direction of the magnetic field, one can modify the number of spectrally overlapping groups (e.g. groups B, C in Fig. 1E) and hence the effective density of spins. To directly probe the interaction strength within our system, we perform a double electron-electron resonance (DEER) measurement between two spectrally separated NV groups, A and B (Fig. 2A, bottom inset). In this measurement the spin echo protocol decouples group A from slowly varying magnetic noise. However, the additional π -pulse on group B after half of the total evolution ensures that the dephasing induced by interactions between the two groups is not decoupled. As depicted in Fig. 2A, by comparing the decay of group A with and without the π -pulse, this measurement allows us to extract the interaction strength $\sim (2\pi) 420$ kHz (17). To further verify that the additional dephasing originates from inter-group interactions, we fix the total evolution time and vary the frequency, ω , of the group B π -pulse, observing a clear resonance when $\omega = \omega_0^B$ (Fig. 2A top inset). By tuning additional NV groups into spectral resonance, we can confirm that the spin dynamics are dominated by interactions. As a function of the number of resonant groups, ν , we find a total dephasing rate, $\gamma_T = \gamma_b + \nu\gamma_0$, with $\gamma_b \approx 0.9$ MHz and $\gamma_0 \approx 0.4$ MHz, consistent with 45 ppm NV center density (Fig. 2B) (17). The dephasing time of a single group is therefore determined by both interactions within the group and effects from other spin impurities in the lattice. The linear dependence of γ_T on ν indicates that the dephasing is limited by coherent interactions.

Central to our thermalization experiments is the ability to tune both the disorder strength and interactions. This is achieved by using spin-locking and Hartman-Hahn (HH) resonances, both of which rely upon continuous microwave driving resonant with the $|m_s = 0\rangle \rightarrow |m_s = -1\rangle$

transitions of the respective NV groups (20–22). For excitation with Rabi frequency Ω , this defines a “dressed-state” basis, $|\pm\rangle \approx (|m_s = 0\rangle \pm |m_s = -1\rangle)/\sqrt{2}$. In the rotating frame, the energies of these two states are split by the effective on-site potential $\sqrt{\Omega^2 + \delta_i^2}$, where δ_i is the local disorder potential for spin i (of order W). In the limit of strong driving $\Omega \gg \delta_i$, we obtain an effective disorder potential $\tilde{\delta}_i$ with the reduced width $W_{\text{eff}} \sim W^2/\Omega$, allowing us to tune the disorder by simply adjusting the Rabi frequency. For spin-locking, we initialize NVs along the \hat{x} -axis via a $\pi/2$ -pulse around the \hat{y} -axis, thereby polarizing spins in the dressed-state basis. Following coherent driving around the \hat{x} -axis for time τ , an additional $\pi/2$ -pulse allows the measurement of the polarization in this basis (Fig. 2C). Figure 2D shows a spin-lock experiment performed at two Rabi frequencies. In comparison to the spin coherence time obtained from a spin-echo measurement, we observe a dramatic enhancement of the lifetime. We find that the lifetime is limited by interactions with short-lived spins in our system, which is suppressed by increasing Ω (23). Thus, spin-locking enables us to prepare a single group of polarized NVs with tunable disorder and long lifetime.

This provides an ideal starting point to probe dipolar thermalization dynamics. In particular, we utilize Hartmann-Hahn (HH) resonances to control the cross-relaxation between two groups of NVs. The two groups are initialized along $+\hat{x}_A$ (group A) and $-\hat{x}_B$ (group B), and spin-locked with Rabi frequencies Ω_A and Ω_B (Fig. 3A). This prepares two oppositely polarized spin ensembles in the dressed-state basis with typical energy splittings Ω_A and Ω_B . The interaction between the groups results in spin exchange and leads to a resonant cross-relaxation when $\Omega_A = \Omega_B$ (HH condition) (20–22). Figure 3B depicts the results of a spin-lock measurement on group A as a function of Ω_B , revealing a sharp resonance. The linewidth of this resonance can be monitored as a function of the common Rabi frequency $\Omega = \Omega_A = \Omega_B$ (Fig. 3B inset), showing a strong decrease for higher driving strength caused by a reduction of the effective disorder (Fig. 3C). To characterize the dynamics of the cross-relaxation, we record the population decay

of group A under HH condition and normalize it by a sufficiently detuned case (17). We observe a decay profile that fits neither a diffusive power law ($\sim t^{3/2}$) nor a simple exponential (Fig. 3D). Repeated with various driving strengths Ω , we find that the polarization decays faster for higher Rabi frequencies, consistent with a smaller effective disorder (Fig. 4A).

To understand these observations, we turn to a theoretical description of our system. Spin dynamics are governed by the interplay between disorder and long-range dipolar interactions. Working in the dressed state basis with quantization axis along \hat{x} , we find that the form of this interaction depends on whether spins reside in the same or distinct groups. For spins in different groups (A and B), dipolar interactions naturally lead to exchange, $H_{AB} = \sum_{i \in A, j \in B} J_{ij}/r_{ij}^3 (\sigma_i^+ \sigma_j^- + \sigma_i^- \sigma_j^+)$, where r_{ij} is the distance between spins, J_{ij} is the orientation dependent coefficient of the dipolar interaction with typical strength $J_0 = (2\pi) 52 \text{ MHz}\cdot\text{nm}^3$, and $\sigma_i^\pm = \sigma_i^y \pm i\sigma_i^z$. However, for spins in the same group (17), the $S = 1$ nature of the NV centers and energy conservation in the rotating frame, lead to an absence of spin exchange; rather, the coupling between spins takes the form of an Ising interaction, $H_{A(B)} = \sum_{i,j \in A(B)} J_{ij}/r_{ij}^3 \sigma_i^x \sigma_j^x$. This observation provides a useful starting point to study cross-relaxation dynamics: when two groups are oppositely polarized, a spin may only depolarize through exchange with spins of the opposite group. Specifically, in the limit of strong disorder, one expects the dynamics to be dominated by rare resonant exchange processes between the two groups. To describe such dynamics, we consider a simplified model, where a single group A excitation is located at the center of an ensemble of polarized group B spins (Fig 4B). The dynamics of this excitation are captured by an effective Hamiltonian,

$$H_{\text{eff}} = \sum_i \tilde{\delta}_i \sigma_i^x - \sum_{ij} \frac{J_{ij}}{r_{ij}^3} (\sigma_i^+ \sigma_j^- + h.c.). \quad (1)$$

where $\tilde{\delta}_i = \sqrt{\Omega^2 + \delta_i^2} - \Omega$ is the effective disorder potential. While this single-particle model neglects both intra-group Ising interactions and the intrinsic dynamics of the on-site disorder

field, it captures key features of slow relaxation in critical systems; these additional features will be necessary to accurately describe the long time thermalization behavior.

To characterize the spin decay dynamics governed by H_{eff} , we calculate the survival probability, $P(t)$, of the excitation via a combination of analytic resonance counting and numerical simulations. For a given disorder realization, this resonance counting proceeds as follows. Two spins at sites i and j are on resonance at time t if: (1) their energy mismatch is smaller than their dipolar interaction strength, $|\tilde{\delta}_i - \tilde{\delta}_j| < \beta J_{ij}/r_{ij}^3$ (β is a dimensionless constant of order unity), and (2) the interaction occurs within the time-scale t , $J_{ij}/r_{ij}^3 > 1/t$ (12). $P(t)$ is approximately given by the probability of having found no resonances up to time t or equivalently up to distance $R(t) \equiv (J_0 t)^{1/3}$ (17). This probability can be computed as the product of probabilities of having no resonant spins at each distance r ,

$$P(t) = \prod_r^{R(t)} \left(1 - 4\pi n r^2 dr \frac{\beta J_0 / r^3}{W_{\text{eff}}} \right) \propto t^{\frac{-4\pi n \beta J_0}{3W_{\text{eff}}}}. \quad (2)$$

$P(t)$ exhibits power-law decay with a disorder dependent exponent $\eta = 4\pi n \beta J_0 / (3W_{\text{eff}})$. This sub-exponential relaxation is the essence of the slow critical dynamics predicted by Anderson (1). Such single-particle power-law relaxation is consistent with results obtained from random-banded matrix theory (15, 24) and is numerically verified for up to $N = 10^4$ spins (Fig. 4C). Furthermore, intra-group Ising interactions among multiple spin excitations can be incorporated into the theory at the level of a mean-field description. In particular, each spin experiences an on-site Ising field, $\delta_i^I \equiv \sum_j J_{ij}/r_{ij}^3 \langle \sigma_j^x \rangle$. When the spins are polarized, owing to the random positioning of NVs, δ_i^I behaves as an additional disorder with characteristic strength $J/4 \sim (2\pi) 105 \text{ kHz}$.

A detailed comparison of our experimental observations with these theoretical predictions is shown in Fig. 4. At short times ($t < 2 \mu\text{s}$), we observe a small but rapid drop in polarization, as the effective quantization axis is perturbed by off-resonant interactions. Over the next decade

($2 \mu\text{s} < t < 20 \mu\text{s}$), we find that relaxation follows a power law, exhibiting a disorder-dependent exponent. The extracted exponents are generally consistent with those predicted by the theory (Fig. 4D). However, we find that the inclusion of the effective Ising field is important to obtain good agreement with experiment. Unlike tunable disorder $\tilde{\delta}_i(\Omega)$, the Ising field, δ_i^I , is not suppressed at large Ω , thereby slowing down relaxation and leading to a saturation of the power-law exponent, in agreement with our experimental observations.

At late times ($t > 20 \mu\text{s}$), the observed decay accelerates and deviates significantly from the power law predicted by our simple description. This deviation can be explained by taking into account the time-dependence of the disorder potential. The microscopic origin of such time-dependence can arise from two sources: evolution of the Ising field, $\delta^I(t)$, induced by depolarization and fluctuations of the on-site disorder field, $\tilde{\delta}(t)$, caused by dynamics associated with coupling to a bath of magnetic impurities. Intuitively, time-dependent disorder can enhance relaxation because a pair of initially off-resonant spins may come into resonance as the local potentials vary in time. To describe this, we modify our model by assuming that the on-site disorder potential consists of both a static part and a dynamic part with standard deviations W_s and W_d . We assume that the dynamic disorder fluctuates at rate $1/\tau_d$. The survival probability $P(t)$ can then be computed using a modified resonance condition where two spins are considered resonant at time t , if at any prior time t' , their energy mismatch is smaller than their dipolar interaction strength, $|\tilde{\delta}_i(t') - \tilde{\delta}_j(t')| < \beta J_{ij}/r_{ij}^3$ (17). From the experimental observations, one can extract W_d and τ_d as a function of Ω . The resulting $P(t)$ is shown in Fig. 4A and is in quantitative agreement with the data over all time scales. Interestingly, we find that in limit of large Ω , the amplitude of the dynamical disorder saturates at $W_d \sim (2\pi) 99 \pm 12 \text{ kHz}$, comparable to the strength of Ising interactions, while the fluctuation time scale $\tau_d \sim 80 \mu\text{s}$ (17, 23, 25) is consistent with the measured NV depolarization time. This suggests that the dynamical disorder is dominated by intrinsic contributions from Ising interactions, which is related to the

predicted thermalization enhancement due to multi-particle resonances and higher order processes (12, 16).

We have demonstrated that dense ensembles of NV centers constitute a powerful platform for exploring quantum dynamics of strongly correlated many body systems with controllable disorder and interactions. Complementary to recent studies of localization in cold atomic systems (9–11), these spin systems exhibit slow, disorder-dependent relaxation associated with critical thermalization dynamics in 3D dipolar systems. The agreement between observed spin relaxation and resonance counting demonstrates that the dynamics are dominated by rare resonances. Moreover, the observed deviations from simple theory demonstrate the subtle role that many-body effects and coupling to the environment can play in such systems. In particular, our analysis demonstrates that Ising interactions play a dual role in the thermalization process, suppressing dynamics at short times (9), while enhancing relaxation at long times. These studies can be extended along several directions. A higher degree of spatial quantum control can be obtained via spin-based sub-wavelength imaging techniques (26). Advanced dynamical decoupling techniques can enable the engineering of a broader class of interaction Hamiltonians and the direct measurement of quantum entanglement dynamics (27, 28). The use of strong magnetic field gradients or the fabrication of diamond nanostructures can allow for the exploration of spin dynamics in lower dimensional systems (18). In combination, these directions may enable the study of the dynamical quantum phase transition from localization to thermalization (9, 10, 29, 30) and open up new opportunities for controlling quantum states in such complex interacting systems (31, 32).

References and Notes

1. P. W. Anderson, *Physical Review* **109**, 1492 (1958).

2. D. S. Wiersma, P. Bartolini, A. Lagendijk, R. Righini, *Nature* **390**, 671 (1997).
3. T. Schwartz, G. Bartal, S. Fishman, M. Segev, *Nature* **446**, 52 (2007).
4. G. Roati, *et al.*, *Nature* **453**, 895 (2008).
5. J. Billy, *et al.*, *Nature* **453**, 891 (2008).
6. D. Basko, I. Aleiner, B. Altshuler, *Annals of Physics* **321**, 1126 (2006).
7. V. Oganesyan, D. A. Huse, *Physical Review B* **75**, 155111 (2007).
8. A. Pal, D. A. Huse, *Physical Review B* **82**, 174411 (2010).
9. M. Schreiber, *et al.*, *Science* **349**, 842 (2015).
10. J.-y. Choi, *et al.*, *Science* **352**, 1547 (2016).
11. J. Smith, *et al.*, *Nature Physics* (2016).
12. N. Y. Yao, *et al.*, *Physical Review Letters* **113**, 243002 (2014).
13. L. Levitov, *EPL (Europhysics Letters)* **9**, 83 (1989).
14. L. Levitov, *Physical Review Letters* **64**, 547 (1990).
15. V. Kravtsov, O. Yevtushenko, P. Snajberk, E. Cuevas, *Physical Review E* **86**, 021136 (2012).
16. A. L. Burin, *arXiv preprint cond-mat/0611387* (2006).
17. Materials and methods are available as supporting material on science online.
18. M. J. Burek, *et al.*, *Nano Letters* **12**, 6084 (2012).
19. G. Balasubramanian, *et al.*, *Nature Materials* **8**, 383 (2009).

20. S. Hartmann, E. Hahn, *Physical Review* **128**, 2042 (1962).
21. C. Belthangady, *et al.*, *Physical Review Letters* **110**, 157601 (2013).
22. P. London, *et al.*, *Physical Review Letters* **111**, 067601 (2013).
23. S. Choi, *et al.*, *arXiv preprint arXiv:1608.05471* (2016).
24. A. D. Mirlin, Y. V. Fyodorov, F.-M. Dittes, J. Quezada, T. H. Seligman, *Physical Review E* **54**, 3221 (1996).
25. J. Cardellino, *et al.*, *Nature Nanotechnology* **9**, 343 (2014).
26. P. Maurer, *et al.*, *Nature Physics* **6**, 912 (2010).
27. P. Hauke, M. Heyl, L. Tagliacozzo, P. Zoller, *Nature Physics* (2016).
28. M. Serbyn, *et al.*, *Physical Review Letters* **113**, 147204 (2014).
29. T. Langen, *et al.*, *Science* **348**, 207 (2015).
30. E. Kaminishi, T. Mori, T. N. Ikeda, M. Ueda, *Nature Physics* **11**, 1050 (2015).
31. S. Choi, N. Y. Yao, S. Gopalakrishnan, M. D. Lukin, *arXiv preprint arXiv:1508.06992* (2015).
32. N. Y. Yao, C. R. Laumann, A. Vishwanath, *arXiv preprint arXiv:1508.06995* (2015).

Acknowledgments: We thank A. Gali, D. Budker, B. J. Shields, A. Sipahigil, M. Knap, S. Gopalakrishnan and J. Chalker for insightful discussions and N.P. De Leon for fabricating the diamond nanobeam. This work was supported in part by CUA, NSSEFF, ARO MURI, Moore Foundation, Miller Institute for Basic Research in Science, Kwanjeong Educational Foundation, Samsung Fellowship, NSF PHY-1506284, NSF DMR-1308435, Japan Society for the

Promotion of Science KAKENHI (No. 26246001), EU (FP7, Horizons 2020, ERC), DFG, Volkswagenstiftung and BMBF.

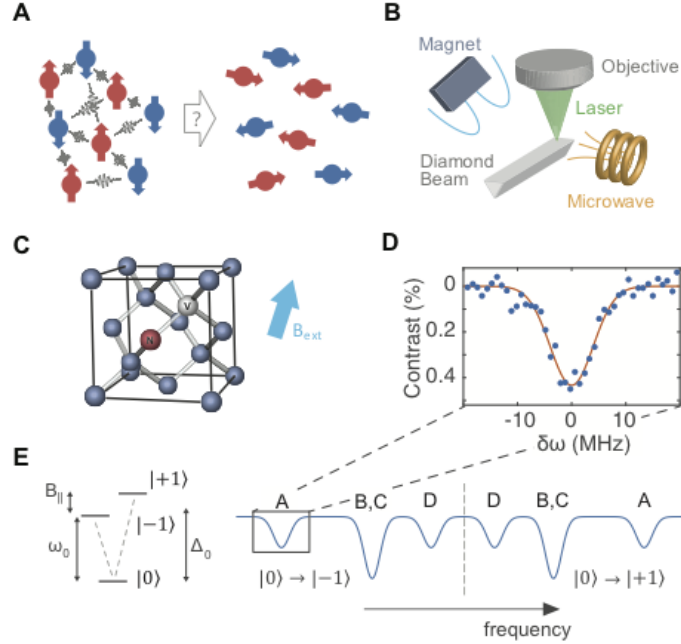


Figure 1: Experimental System. (A) Schematic depicting two groups of oppositely polarized spins with local variation of transition frequencies. Due to long-range dipolar interactions, such a system will eventually thermalize to an unpolarized spin state. (B) Experimental setup diagram showing a diamond nanobeam containing nitrogen vacancy centers, confocally addressed via a 532 nm laser. External magnetic fields as well as pulsed microwave radiation are used to control the defect's spin degrees of freedom. (C) The crystallographic structure of diamond contains four possible NV quantization axes, defined by the position of the nitrogen atom and the adjacent vacant lattice site. A NV ensemble in diamond therefore consists of four groups {A, B, C, D}. An external magnetic field (B_{ext}) is used to split each group's spin degrees of freedom. (D) ESR scan of a single transition of NV spins (blue points). Red solid line represents a Gaussian fit with standard deviation W , corresponding to the average disorder in the sample. (E) Simplified NV level scheme showing the spin degrees of freedom in the optical ground state. A large zero-field splitting Δ_0 in combination with a magnetic field induced Zeeman shift leads to individual addressability of the spin sub-levels. The solid blue line shows a schematic representation of an ESR scan, revealing the spin transitions of all four NV groups. Here, the orientation of the external magnetic field is chosen in such a way that NV group B and C experience the same magnetic field projection (B_{\parallel}), leading to spectral degeneracy.

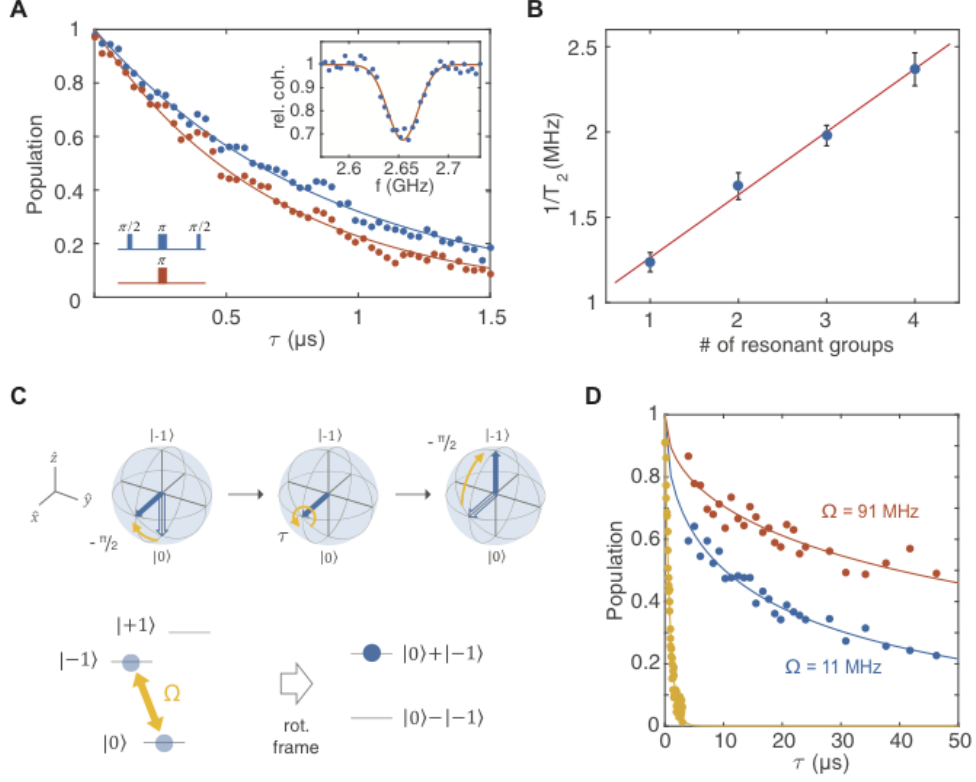


Figure 2: Interacting Spin Ensemble. (A) Spin echo on NV group A (blue points) and double electron-electron resonance scan on group A and B (red points). Solid lines indicate exponential fits to the data. Inset shows the relative spin-echo coherence time at a fixed time τ as a function of driving frequency of group B. (B) Spin echo coherence time as a function of resonant NV groups. (blue points). The red solid line represents a linear fit to the data. Errorbars correspond to 1σ . (C) Schematic diagram depicting a spin-lock sequence. An initial $-\pi/2$ pulse around the y-axis is followed by continuous driving around the x-axis. This creates a dressed spin basis with the two eigenstates $(|m_s = 0\rangle + |m_s = -1\rangle)/\sqrt{2}$ and $(|m_s = 0\rangle - |m_s = -1\rangle)/\sqrt{2}$. Another $-\pi/2$ pulse around the y-axis is subsequently used to convert the acquired phase back into population. (D) Spin-lock coherence decay for low (blue points) and high CW driving power (red points) showing significant extension beyond the spin echo coherence time (orange points). The decay curves are fitted to a stretched exponential function $\exp[-\sqrt{t/T}]$ (23).

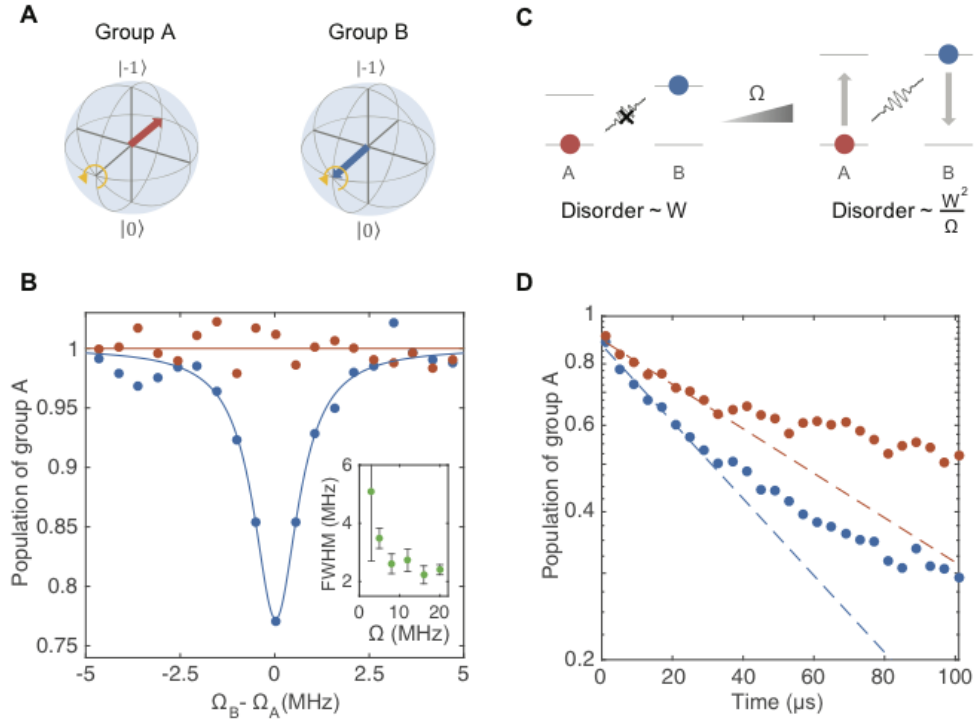


Figure 3: Spin Cross-Relaxation. (A) Schematic diagram depicting opposite phase spin-lock driving of two separate groups of NVs (A and B) leading to two oppositely polarized groups of spins in the dressed state spin basis. By matching the two driving powers resonant population transfer (Hartmann-Hahn condition) can be achieved. (B) Population of group A in a double spin-lock sequence as a function of driving power of group B, showing the Hartmann-Hahn resonance (blue points). Red data shows spin-lock coherence without driving of other groups. The solid blue curve represents a Lorentzian fit to the data. Inset shows the resonance linewidth as a function of applied Rabi frequency. Errorbars correspond to 1σ . (C) Diagram showing that increasing the common Rabi frequency reduces the effective disorder of the system leading to more efficient spin transfer. (D) Population dynamics of group A at the Hartmann-Hahn resonance condition (blue data) as well as at a detuning of 1 MHz (red data) as a function of evolution time. Dashed lines represent exponential guides to the eye, showing significant deviation at long times.

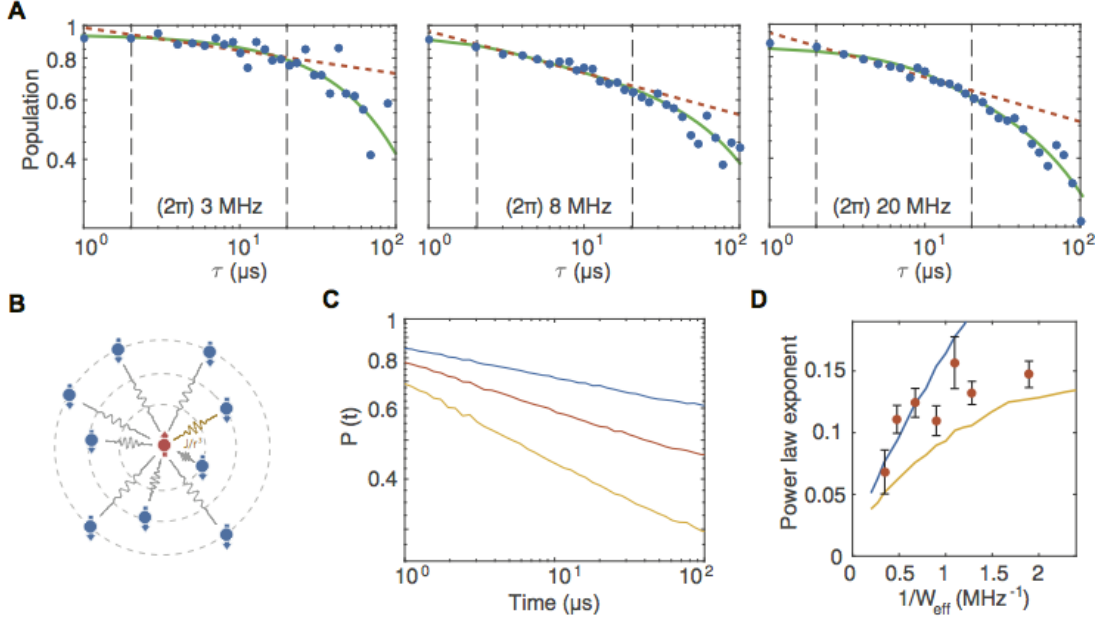


Figure 4: Thermalization Dynamics. (A) NV polarization decay under Hartmann-Hahn conditions for three different driving strengths. Dashed black lines indicate the intermediate regime over which the power law (dashed red line) is fit. Green solid line indicates Monte-Carlo fit of our model including time dependent disorder. We extract $W_d = (2\pi)$ $[120 \pm 20, 230 \pm 15, 86 \pm 5]$ kHz, and $\tau_d = [6 \pm 5, 48 \pm 8, 73 \pm 18]$ μs for $\Omega = (2\pi)[3, 8, 20]$ MHz, respectively. (B) Schematic diagram of single particle resonance counting argument predicting a power-law decay profile. (C) Exact diagonalization simulation results for a simplified single excitation model showing power-law decay shape for three different driving strengths, (2π) $[3, 8, 20]$ MHz. Solid lines indicate the intermediate time over which a power-law decay is observed in the experiment data. (D) Exponent of the power-law decay as a function of decreased effective disorder (red points). Orange/blue points correspond to simulation results with/without the addition of Ising interaction.

Supplementary Materials for Critical thermalization of a disordered dipolar spin system in diamond

G. Kucsko,^{1†} S. Choi,^{1†} J. Choi,^{1,2†} P. C. Maurer,³ H. Sumiya,⁴ S. Onoda,⁵
J. Isoya,⁶ F. Jelezko,⁷ E. Demler,¹ N. Y. Yao,⁸ M. D. Lukin^{1*}

[†]These authors contributed equally to this work.

*To whom correspondence should be addressed

E-mail: lukin@physics.harvard.edu

Contents

1	Materials and Methods	2
1.1	Sample Fabrication	2
1.2	Optical Setup	3
1.3	Microwave Setup	3
1.4	Magnetic Field Setup	5
2	Characterization of Experimental System	6
2.1	On-site Potential Disorder	6
2.2	Estimation of NV Density and Dipolar Interaction Strength	9
2.3	Inhomogeneity of the Microwave Field	10
3	Effective Hamiltonian of a Driven System	12
4	Resonance Counting Theory	16

4.1	Disorder-dependent Power-law Decay	16
4.2	Time-dependent Disorder	18
5	Detailed Analysis of Thermalization Experiments	19
5.1	Effects of Incoherent Dynamics	19
5.2	Comparison with Theory	21
5.3	Dependence of Spin Cross-relaxation on Initial Spin States	22

1 Materials and Methods

1.1 Sample Fabrication

The diamond sample used in this work (type-Ib, ~ 4 mm in diameter) was grown via high pressure and high temperature (HPHT), at 5.5 GPa and 1350 °C, using a Fe-Co alloy as a solvent. The main source of paramagnetic impurities was provided by substitutional nitrogen atoms in the neutral charge state (P1 centers) at a concentration of ~ 100 ppm. A diamond plate of thickness ~ 1 mm was obtained via laser cutting and polishing. To obtain NV centers, high energy electron irradiation was performed at ~ 2 MeV with a flux of $1.3\text{-}1.4 \cdot 10^{13} \text{ e} \cdot \text{cm}^{-2} \cdot \text{s}^{-1}$ and in-situ annealing at 700-800 °C up to a total fluence of $1.4 \cdot 10^{19} \text{ cm}^{-2}$ (total time of 285 hrs). Additional annealing at 1000 °C for 2 hrs in vacuum was performed after half as well as after the full irradiation time. This process resulted in the diamond with NV centers of a concentration ~ 45 ppm, corresponding to ~ 5 nm of average separation and $\sim (2\pi) 420$ kHz dipole-dipole interaction strength. To control the region of optical excitation, we used angle etching to create a beam-shaped piece of diamond, of $20 \mu\text{m}$ length and ~ 300 nm width, and transferred it onto our coplanar waveguide (1).

1.2 Optical Setup

As shown in Fig. S1A, the optical setup consists of a home-built confocal microscope with a Nikon Plan Fluor 100x oil immersion objective (NA = 1.3). The sample is mounted on a xyz-piezoelectric stage in the focal plane of the microscope. Excitation of the ensemble of NV centers is performed by illuminating a green laser ($\lambda = 532$ nm) with average power less than $50 \mu\text{W}$. Short laser pulses are generated by an acousto-optic modulator (AOM) from Isomet in a double pass configuration. The $\lambda/2$ -waveplate at the objective allows the control over the polarization of excitation light. NV centers emit fluorescence into the phonon sideband (630-800 nm), which is isolated from the excitation laser by a dichroic mirror. An additional 650 nm long-pass filter further suppresses the detection of unwanted signal. After passing a pinhole the collection beam is then focused onto a single photon counting avalanche photodiode (APD) to achieve detections with confocal resolution.

To probe the spin dynamics over time, we used a pulse sequence illustrated in Fig. S1B. We repeat the same pulse sequence twice, but include an extra π -pulse right before the read-out at end of the second sequence. The photon-count difference between the two read-outs allows us to measure the NV polarization, while being insensitive to changes in the background fluorescence due to charge dynamics (2).

1.3 Microwave Setup

To coherently control the electronic spin states of NV centers we deliver microwaves to the sample through an impedance-matched coplanar waveguide fabricated on a glass coverslip. An omega-shaped microstructure (with a inner diameter $20 \mu\text{m}$) at the center of the waveguide allows us to achieve Rabi frequencies up to $\sim(2\pi) 100$ MHz. In Fig. S2, we illustrate the schematic diagram of the microwave control system. In order to have full control over two groups of NV centers with different transition frequencies, we employ two independent

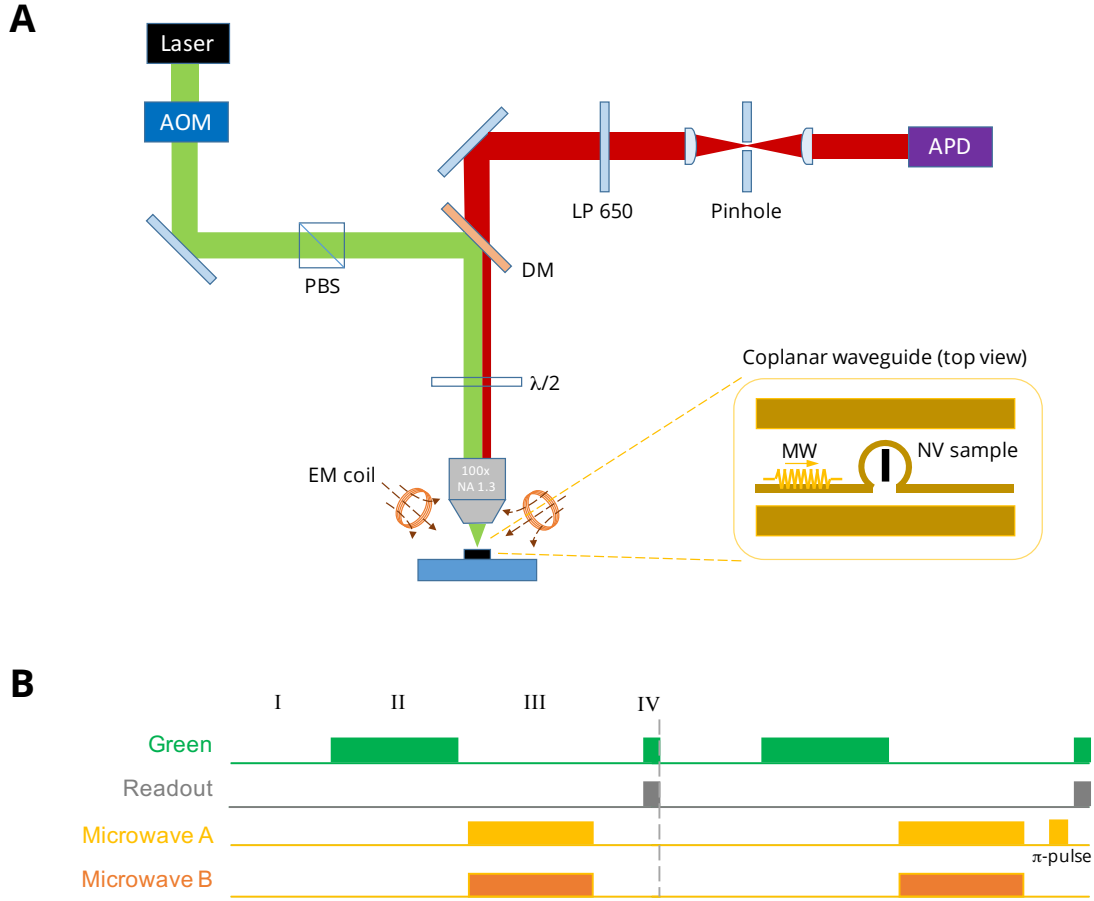


Figure S1: Schematic of the Optical Setup and the Pulse Sequence. (A) Green and red lines indicate the optical paths (excitation: green, collection: red). An acousto-optic modulator (AOM) is used to control green laser duration. A dichroic mirror (DM) spectrally filters out the fluorescence from NV centers for electronic spin state readout. A 650 nm long pass filter additionally helps to filter fluorescence emission, corresponding to the phonon sideband (PSB) of NV centers. A 5- μm pinhole is used in combination with a single photon counting avalanche photodiode (APD) to achieve confocal detection. A polarizing beam splitter (PBS) is used to polarize the excitation beam. With the addition of a $\lambda/2$ waveplate we get control over the incident green polarization onto the diamond sample. The sample is placed on top of a coplanar microwave (MW) structure in the shape of an omega (inset). Three electromagnetic coils are used to create a static magnetic field up to ~ 300 Gauss in an arbitrary direction. (B) Typical experimental sequence used to measure NV dynamics. I: charge equilibration; II: spin polarization; III: experimental sequence; IV: spin readout.

microwave circuits. In each circuit, a RF signal generator (Rohde & Schwarz SMIQ06B) produces the main driving frequency; an IQ mixer (Marki IQ1545LMP) generates pulsed signals; a low-pass microwave filter (Mini-Circuits VLF-3000+) suppresses unwanted higher-order harmonics of fundamental frequencies; and a DC block (Picosecond 5501a) additionally isolates the signals from low-frequency noises. After separately amplified (ZHL-16W-43+), two RF signals are then combined by a power combiner (Mini-Circuits ZFRSC-42-S+) and delivered to our sample. The inset of Fig. S2 depicts the detailed configuration of analog inputs (AI) connected to the IQ mixers. An arbitrary waveform generator (The Tektronix AWG7052) defines the duration and the phase of the pulses with a temporal resolution of 1 ns. For fine tuning of the voltage offset on the I and Q ports, a DC voltage is applied to the AWG signal. The addition of a 10-dB attenuator between the voltage source and the combiner suppresses unwanted reflections (see inset of Fig. S2).

1.4 Magnetic Field Setup

For an external magnetic field, we use three water-cooled electromagnetic (EM) coils, which can provide a B-field up to ~ 300 Gauss in an arbitrary orientation (see Fig. S1A and S3A).

As shown in Fig. S3B, we calibrate the magnetic field by recording electron spin resonance (ESR) spectra at various values of currents in the coils; since the Hamiltonian of a NV center in the presence of a magnetic field is known, the magnetic field at the position of our sample can be extracted from transitions frequencies of NV centers. For this process we utilize all four groups $\{A, B, C, D\}$ of NV centers oriented in different crystallographic axes of diamond lattice, e.g., $A = [111]$, $B = [\bar{1}\bar{1}1]$, $C = [1\bar{1}\bar{1}]$, and $D = [\bar{1}\bar{1}\bar{1}]$ (see Fig. S3C). Fig. S3D shows an ESR spectrum when the B-field is aligned along $[111]$ direction; group A exhibits the largest Zeeman splitting, while the other groups B, C, and D become degenerate. In Fig. S3E, the direction of an external B-field is perpendicular to the sample surface, i.e., $B \parallel [001]$, resulting

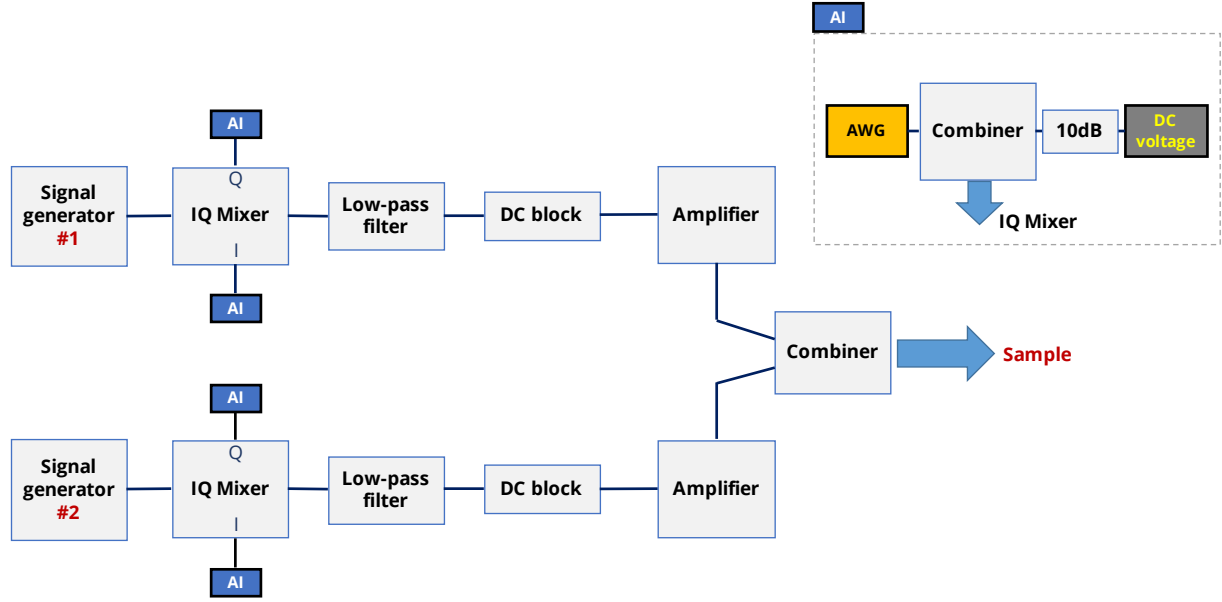


Figure S2: **Schematic of the Microwave Control Setup.** Two sets of independent microwave circuits are used to achieve full control over two separate groups of NV centers at different transition frequencies. A 3 GHz low-pass filter suppresses unwanted higher-order harmonics. The two microwave paths are separately amplified to avoid saturation and then combined and sent to the diamond sample. In order to precisely control the microwave pulse length as well as phase, each path is sent through an IQ mixer controlled by an arbitrary waveform generator (AWG) output. The inset shows the detailed configuration of analog inputs connected to the IQ mixers used to define microwave pulse length and phase. In order to finely tune the voltage offset of the I and Q port, to achieve high isolation, a DC voltage source is combined with the AWG signal. The addition of an attenuator allows the suppression of unwanted reflections.

in four degenerate groups.

2 Characterization of Experimental System

2.1 On-site Potential Disorder

The ESR linewidth of an NV ensembles is influenced by multiple factors. To discuss and estimate their contributions we introduce the ground state hamiltonian of the electronic spin

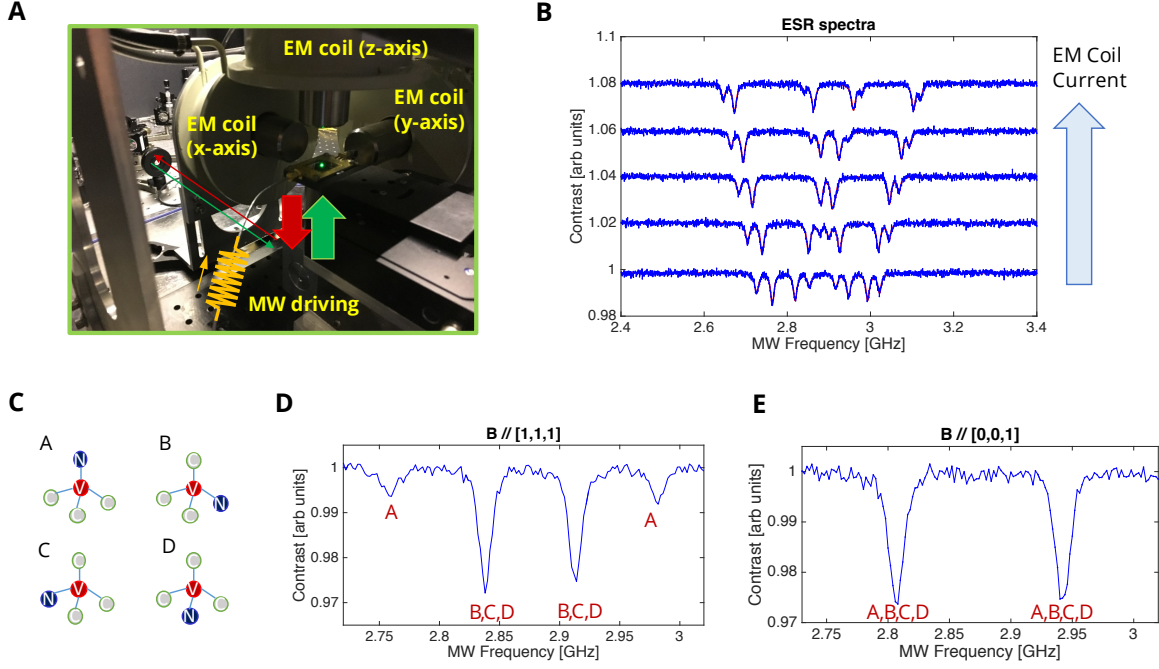


Figure S3: Magnetic Field Calibration and Control. (A) Three electromagnetic (EM) coils are located in the vicinity of the diamond sample in order to provide an external magnetic field (B-field) in an arbitrary direction with an amplitude up to ~ 300 Gauss. (B) To calibrate the coil's magnetic field, electron spin resonance (ESR) spectra are recorded for different values of coil currents. (C) The diamond lattice allows for four different crystallographic orientations of NV centers. The different groups A, B, C, and D of NV centers are characterized by their N-V axis orientations, i.e., $A = [111]$, $B = [\bar{1}\bar{1}1]$, $C = [1\bar{1}\bar{1}]$, and $D = [\bar{1}1\bar{1}]$. (D) Measured ESR spectrum for the B-field aligned along the $[111]$ direction. Group A exhibits the largest Zeeman splitting (highest projected B_{\parallel}) because the spin quantization axis of group A is parallel to the chosen B-field. (E) Measured ESR spectrum for the B-field aligned along the $[001]$ direction. Due to the $[100]$ cutting direction of the diamond, all 4 NV groups form the same angle to the surface. With the external B-field being perpendicular to the sample surface, this leads to groups A-D having degenerate B field projections.

state of a single NV center:

$$H = (\hbar\Delta_0 + d_{\parallel}E_{\parallel}^z) S_z^2 + \gamma_{NV}(\vec{S} \cdot \vec{B}) - d_{\perp} [E_{\perp}^x (S_x S_y + S_y S_x) + E_{\perp}^y (S_x^2 - S_y^2)], \quad (S1)$$

where S_x , S_y and S_z denote the Pauli spin matrices and \hbar the reduced Planck constant; $\Delta_0 \approx (2\pi)2.87$ GHz, $\gamma_{NV} = (2\pi) 2.8$ MHz G $^{-1}$, $d_{\parallel} = (2\pi) 0.35$ Hz cm V $^{-1}$ and $d_{\perp} = (2\pi) 17$ Hz cm

V^{-1} are the zero field splitting, the gyromagnetic ratio, axial and perpendicular components of the ground triplet state permanent electric dipole moment of a NV center (3). $B_{\parallel(\perp)}$ and $E_{\parallel(\perp)}$ are projection of the effective magnetic and electric field parallel (perpendicular) to the NV axis. To a leading order, we ignore the effect of the perpendicular magnetic field noise δB_{\perp} , since it influence less on the spin coherence than the parallel one δB_{\parallel} , owing to the large zero field splitting.

To account for effects of the local NV environment we include in B_{\parallel} and $E_{\parallel(\perp)}$ on-site potential disorders originating from randomly distributed magnetic fields due to nuclear spins (i.e. ^{13}C or ^{14}N) and paramagnetic impurities (i.e. P1 centers) as well as fields caused by local electric fields and lattice strain. To quantify the different contributions to the ESR linewidth, we conduct Ramsey spectroscopy in distinct basis states as listed in Fig. S4A. Since each basis has a well defined sensitivity to different physical noise sources, our Ramsey measurements provide insight into the local environment of the NV centers. Table SI lists the effects of magnetic and electric field noise on free induction decay of several different basis states. Figure S4 shows the outcome of Ramsey spectroscopy in the five different bases defined in SI .

Definition	Wavefunction	Precession rate	Noise	$1/T_2^*$
$ \psi_1\rangle$	$(0\rangle + 1\rangle)/\sqrt{2}$	$\gamma_{NV}B_{\parallel} + d_{\parallel}E_{\parallel}$	$\delta B_{\parallel}, \delta E_{\parallel}$	$\pi[\Gamma_{B_{\parallel}} + \Gamma_{E_{\parallel}}]$
$ \psi_2\rangle$	$(0\rangle + -1\rangle)/\sqrt{2}$	$\gamma_{NV}B_{\parallel} + d_{\parallel}E_{\parallel}$	$\delta B_{\parallel}, \delta E_{\parallel}$	$\pi[\Gamma_{B_{\parallel}} + \Gamma_{E_{\parallel}}]$
$ \psi_3\rangle$	$(1\rangle + -1\rangle)/\sqrt{2}$	$2\gamma_{NV}B_{\parallel}$	δB_{\parallel}	$2\pi\Gamma_{B_{\parallel}}$
$ \psi_4\rangle$	$(0\rangle + D\rangle)/\sqrt{2}$	$d_{\parallel}E_{\parallel} + d_{\perp}E_{\perp}$	$\delta E_{\parallel}, \delta E_{\perp}$	$\pi[\Gamma_{E_{\parallel}} + \Gamma_{E_{\perp}}]$
$ \psi_5\rangle$	$(0\rangle + B\rangle)/\sqrt{2}$	$d_{\parallel}E_{\parallel} + d_{\perp}E_{\perp}$	$\delta E_{\parallel}, \delta E_{\perp}$	$\pi[\Gamma_{E_{\parallel}} + \Gamma_{E_{\perp}}]$

Table SI: Five different basis states used for characterizing the local on-site disorder. The dark ($|D\rangle \equiv (|1\rangle - |-1\rangle)/\sqrt{2}$) and bright states ($|B\rangle \equiv (|1\rangle + |-1\rangle)/\sqrt{2}$) are prepared by applying an off-axis magnetic field perpendicular to an NV symmetry axis. Γ is a noise source-dependent inhomogeneous broadening contributing to the linewidth of the ESR.

As seen in the table SI, each coherent superposition can effectively probe different types of noise components, enabling us to quantify the relative strengths of the on-site potential dis-

order. Using the identity $\Gamma = 1/\pi T_2^*$ and the relations given in the last column of table SI, we can estimate a value for the different noise sources $\Gamma_{B\parallel}$, $\Gamma_{E\parallel}$, and $\Gamma_{E\perp}$. The discrepancy in T_2^* between $|\psi_1\rangle$ and $|\psi_2\rangle$ (as well as $|\psi_4\rangle$ and $|\psi_5\rangle$) in experimental data is presumably due to frequency-dependent field noise. By averaging these results, we can extract the three inhomogeneous broadening factors as $\Gamma_{B\parallel} = 3.78(3)$ MHz, $\Gamma_{E\parallel} = 2.18(8)$ MHz and $\Gamma_{E\perp} = 4.30(13)$ MHz. The measured ESR linewidth $\Gamma_{\text{meas}} = \sqrt{8 \ln 2} W \approx 9.4$ MHz (see Fig. 1D, main text) roughly agrees up to a factor of ~ 1.5 with the calculated $\Gamma_{\text{calc}} \approx 6.0$ MHz. According to this analysis, the random on-site disorder in our sample seems to result from both electric and magnetic fields with comparable weights.

2.2 Estimation of NV Density and Dipolar Interaction Strength

Due to the high density of NVs within our sample, the spin-echo coherence time is limited by interactions, as discussed in the main text. To quantitatively analyze the dependence of decoherence rate on the spin density, we study the dynamics of interacting spins using the exact diagonalization method with the effective Hamiltonian of Eq. (S24). Comparing the numerical result to the experimental data allows us to extract the density of NV spins in our sample.

Specifically, we simulate the time evolution of 12 NV spins under a spin echo pulse sequence protocol. The total NV concentrations selected for simulations are 5, 20, 40, 60, 70, 80 and 100 ppm. We averaged over ~ 500 realizations of positional disorder, resulting in a single smooth coherence curve under the spin echo sequence. We fit the coherence decay with a simple exponential function and extract the decoherence rate, $\gamma_T \equiv 1/T_2$. Fig. S5A summarizes the spin echo simulation results as a function of the number of resonant NV groups (effective density), where a linear dependence of γ_T is identified for all the density values. We model the decoherence rate as $\gamma_T(\nu) = \gamma_b(\nu) + \nu\gamma_0(\nu)$, where ν is the number of resonant NV groups, γ_b and γ_0 are density-dependent, bare and dipolar interaction-induced dephasing rates, respec-

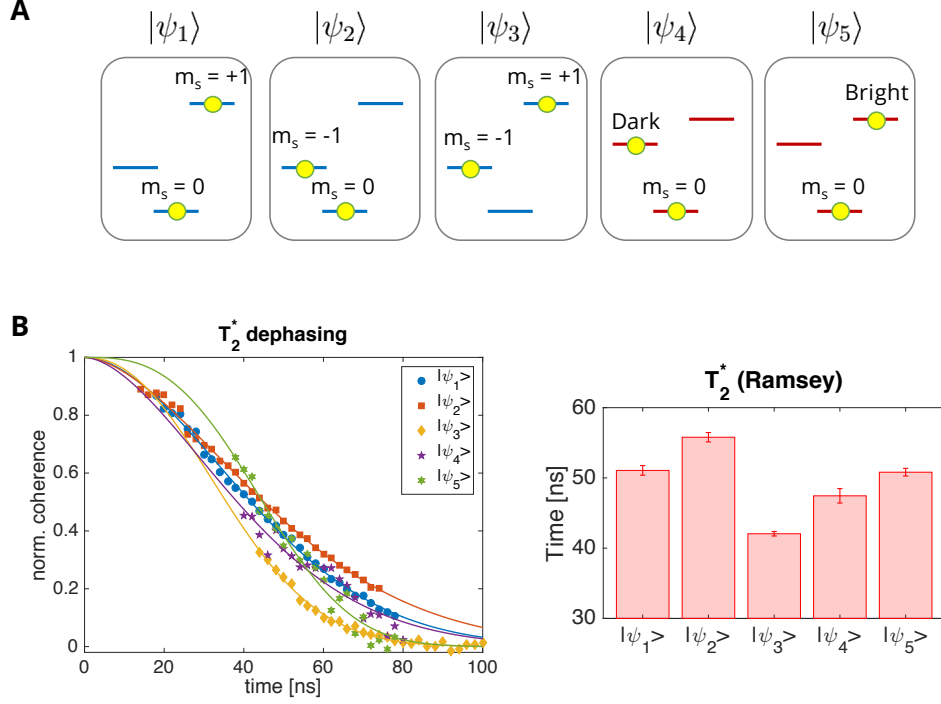


Figure S4: T_2^* and T_2 Measurements of different Basis States. (A) Different initial conditions used for coherence measurements. By aligning the magnetic field parallel (perpendicular) to the NV axis, the eigenbasis for the spin state of NV centers becomes $\{|m_s = 0\rangle, |m_s = +1\rangle, |m_s = -1\rangle\}$ ($\{|m_s = 0\rangle, |Dark\rangle, |Bright\rangle\}$), where Bright and Dark states are defined as even and odd combination of the original bare spin states $|m_s = -1\rangle$ and $|m_s = +1\rangle$. (B) Ramsey spectroscopy data and extracted decay timescale for different initial states.

tively. Such linear dependence of γ_T on ν is also confirmed in the experiment (see Fig. 2B in main text). By comparing γ_0 between the experiment and the simulation, we estimate the NV density in our sample to be ~ 45 ppm (see Fig. S5B).

2.3 Inhomogeneity of the Microwave Field

Hartmann-Hahn resonances rely on the exact matching of Rabi frequencies of two driving fields $\Omega_A = \Omega_B$. Hence, stable and precise control of the driving strength is essential in our experiments. To this end, we estimate the inhomogeneity of our microwave driving field, by measuring

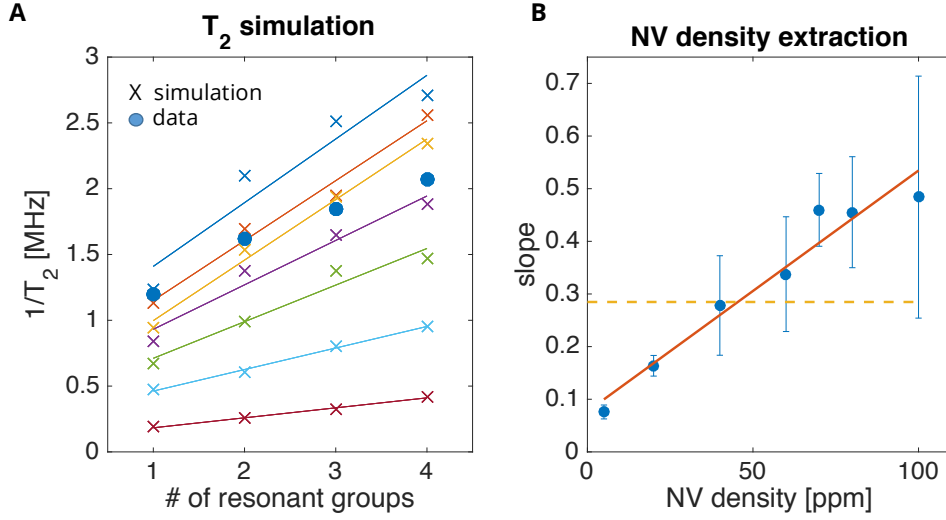


Figure S5: **NV Density Extraction via Spin Echo Simulation.** (A) Comparison of the spin echo simulation results at different concentrations (crosses) to the measured data (circles). The total NV concentrations selected for the simulation are 5, 20, 40, 60, 70, 80 and 100 ppm. Solid lines are linear fits to the simulation to extract both γ_b and γ_0 in the main text. (B) The NV concentration can be extracted by comparing the slopes (γ_0) taken from the numerical simulations to the extracted slope of the experiment data (orange dashed line).

the decay time of Rabi oscillations at various driving strengths (Fig. S6).

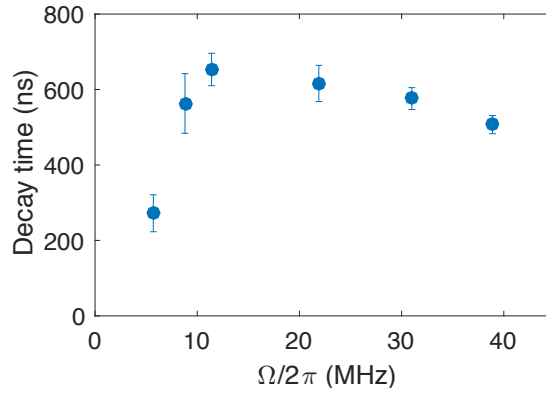


Figure S6: **Rabi Oscillation Measurement.** Decay time of Rabi oscillations as a function of Rabi frequency Ω .

In an ideal case, the lifetime of Rabi oscillations generally increases due to suppression of

disorder (T_2^*). At higher driving strength ($W_{\text{eff}} \sim \delta^I$) this lifetime should saturate due to the effect of Ising interaction. In our measurements however we observe a slight decrease in lifetime at high driving strengths, which is well explained by a 1.1% variation in Rabi frequency. We attribute this variation to spatial inhomogeneity in the driving field. With the strongest driving in our measurement $\Omega = (2\pi) 32$ MHz, this effect leads to a spread in Rabi frequencies of $\sim (2\pi) 0.3$ kHz. While it is still smaller than the effective disorder $\sim (2\pi) 0.6$ kHz, such an inhomogeneity ultimately limits the maximum driving strength of our thermalization experiments.

3 Effective Hamiltonian of a Driven System

In this section, we derive the effective Hamiltonian for a driven, dipolar interacting spin ensemble. The main idea is to work in a frame that is rotating along each NV group's quantization axis at corresponding driving frequency (ω_0^A and ω_0^B for group A and B, respectively). If the difference between ω_0^A and ω_0^B is large compared to the interaction strength, then one can ignore exchange interactions between spins from different groups (secular approximation). This results in distinct forms of intra- and inter-group interactions. We project the original Hamiltonian into two-level systems, and derive the effective Hamiltonian.

We start with the Hamiltonian for dipolar interacting NV centers

$$H = \sum_i H_i^0 + \sum_i H_i^d(t) + \sum_{ij} H_{ij}^{dd}, \quad (\text{S2})$$

where H_i^0 is a single particle Hamiltonian for a spin at site i , $H_i^d(t)$ is time-dependent driving, and H_{ij}^{dd} is the magnetic dipole-dipole interaction between spins at sites i and j . The first term H_i^0 includes Zeeman coupling to an external magnetic field, the zero field splitting of a NV center, and any other disordered potentials arising from couplings to paramagnetic impurities as described in the main text. In our experiments, dominant contributions for H_i^0 come from

the zero-field splitting $\sim (2\pi) 2.87\text{GHz}$ and Zeeman field projected along the quantization axis (a few hundred MHz), which are two orders of magnitude larger than the rest of the couplings. Setting $\hbar = 1$, we can write

$$H_i^0 \approx (\Delta_0 + \delta_{0,i}) (\hat{c}_i \cdot \vec{S}_i)^2 + (\Delta_B(\hat{c}_i) + \delta_{B,i}) (\hat{c}_i \cdot \vec{S}_i) \quad (\text{S3})$$

where \vec{S}_i are spin-1 vector operators, \hat{c}_i is the unit vector along the quantization axis of the spin, $\Delta_0 = (2\pi) 2.87 \text{ GHz}$ is the zero-field splitting, $\Delta_B(\hat{c}_i)$ is the Zeeman splitting along \hat{c}_i , and $\delta_{0,i}$ and $\delta_{B,i}$ are on-site disorder potentials. If the external magnetic field \vec{B} is oriented in a way that $\Delta_B(\hat{c}_i)$ for different groups are sufficiently separated (compared to the driving strength), one can effectively address distinct groups independently. Below we assume such a case and consider resonant driving of two groups A and B using microwave frequencies $\omega_0^{A(B)} = \Delta_0 - \Delta_B(\hat{c}_{A(B)})$. The Hamiltonian for such driving is given as $H_i^d(t) = \gamma_{NV} \vec{B}_{\text{MW}} \cdot \vec{S}_i \cos(\omega_0 t)$, where γ_{NV} is the gyromagnetic ratio of the NV center, and \vec{B}_{MW} is the microwave field vector. Now moving into the rotating frame with unitary transformation $U(t) = \exp \left[-i \left(\sum_i \Delta_0 (\hat{c}_i \cdot \vec{S}_i)^2 + \Delta_B(\hat{c}_i) (\hat{c}_i \cdot \vec{S}_i) \right) t \right]$ and applying rotating wave approximations, we obtain the effective single particle Hamiltonian

$$\bar{H}_i = U^\dagger(t) [H_i^0 + H_i^d(t)] U(t) - iU^\dagger \frac{d}{dt} U \quad (\text{S4})$$

$$= (\delta_{0,i} + \delta_{B,i}) |1\rangle \langle 1| + (\delta_{0,i} - \delta_{B,i}) |-1\rangle \langle -1| + \frac{\Omega}{2} (|-1\rangle \langle 0| + h.c.), \quad (\text{S5})$$

where $\{|1\rangle, |0\rangle, |-1\rangle\}$ is the basis of spin states along its quantization axis and Ω is the Rabi frequency of the driving.

The effective interaction among spins can be obtained in a similar way as follows. We start with the dipole-dipole interaction between spin- i and spin- j

$$H_{ij}^{dd} = -\frac{J_0}{r^3} \left(3 \left(\vec{S}_i \cdot \hat{r} \right) \left(\vec{S}_j \cdot \hat{r} \right) - \vec{S}_i \cdot \vec{S}_j \right), \quad (\text{S6})$$

where $J_0 = (2\pi) 52 \text{ MHz} \cdot \text{nm}^3$ and \vec{r} is the relative position between two spins. In the rotating frame, we obtain the effective interaction by replacing $\vec{S}_i \mapsto U^\dagger(t)\vec{S}_i U(t)$. Since we are interested in the interaction in the basis of each NV's own quantization axis, we first explicitly rewrite \vec{S}_i in terms of (S_i^x, S_i^y, S_i^z) in a coordinate system where \hat{z}_i is parallel to the quantization axis \hat{c}_i

$$\bar{H}_{ij}^{dd} = U^\dagger(t) H_{ij}^{dd} U(t) = -J_0/r^3 \left[(3(\hat{r} \cdot \hat{x}_i)(\hat{r} \cdot \hat{x}_j) - \hat{x}_i \cdot \hat{x}_j) S_i^x S_j^x \right. \quad (\text{S7})$$

$$\left. + (3(\hat{r} \cdot \hat{y}_i)(\hat{r} \cdot \hat{y}_j) - \hat{y}_i \cdot \hat{y}_j) S_i^y S_j^y \right. \quad (\text{S8})$$

$$\left. + (3(\hat{r} \cdot \hat{x}_i)(\hat{r} \cdot \hat{y}_j) - \hat{x}_i \cdot \hat{y}_j) S_j^x S_j^y \right. \quad (\text{S9})$$

$$\left. + (3(\hat{r} \cdot \hat{y}_i)(\hat{r} \cdot \hat{x}_j) - \hat{y}_i \cdot \hat{x}_j) S_i^y S_j^x \right. \quad (\text{S10})$$

$$\left. + (3(\hat{r} \cdot \hat{z}_i)(\hat{r} \cdot \hat{z}_j) - \hat{z}_i \cdot \hat{z}_j) S_i^z S_j^z \right] \quad (\text{S11})$$

$$+ H_{\text{rest}}, \quad (\text{S12})$$

where H_{rest} contains all the other terms of the form $S^x S^z, S^y S^z, S^z S^x, S^z S^y$.

We now perform rotating wave approximations. This is very well justified because the typical strength of the interaction is much weaker than the driving frequency $J_0/r^3 \sim (2\pi) 0.4 \text{ MHz} \ll \omega_0^{A,B} \sim (2\pi) 2.5 \text{ GHz}$. First, we note that S^x and S^y operators are rapidly oscillating in time while S^z remains invariant, $[S_i^z, U(t)] = 0$. Therefore, every term in H_{rest} may be safely ignored. Then, introducing

$$g_{ij}^+ = \frac{1}{2} \left[3(\hat{r} \cdot \hat{x}_i)(\hat{r} \cdot \hat{x}_j) - \hat{x}_i \cdot \hat{x}_j + 3(\hat{r} \cdot \hat{y}_i)(\hat{r} \cdot \hat{y}_j) - \hat{y}_i \cdot \hat{y}_j \right] \quad (\text{S13})$$

$$g_{ij}^- = \frac{1}{2} \left[3(\hat{r} \cdot \hat{x}_i)(\hat{r} \cdot \hat{x}_j) - \hat{x}_i \cdot \hat{x}_j - 3(\hat{r} \cdot \hat{y}_i)(\hat{r} \cdot \hat{y}_j) + \hat{y}_i \cdot \hat{y}_j \right] \quad (\text{S14})$$

$$h_{ij}^+ = \frac{1}{2} \left[3(\hat{r} \cdot \hat{x}_i)(\hat{r} \cdot \hat{y}_j) - \hat{x}_i \cdot \hat{y}_j + 3(\hat{r} \cdot \hat{y}_i)(\hat{r} \cdot \hat{x}_j) - \hat{y}_i \cdot \hat{x}_j \right] \quad (\text{S15})$$

$$h_{ij}^- = \frac{1}{2} \left[3(\hat{r} \cdot \hat{x}_i)(\hat{r} \cdot \hat{y}_j) - \hat{x}_i \cdot \hat{y}_j - 3(\hat{r} \cdot \hat{y}_i)(\hat{r} \cdot \hat{x}_j) + \hat{y}_i \cdot \hat{x}_j \right] \quad (\text{S16})$$

$$q_{ij} = 3(\hat{r} \cdot \hat{z}_i)(\hat{r} \cdot \hat{z}_j) - \hat{z}_i \cdot \hat{z}_j, \quad (\text{S17})$$

we can simply rewrite

$$\bar{H}_{ij}^{dd} \approx -J_0/r^3 [g_{ij}^+(S_i^x S_j^x + S_i^y S_j^y) + h_{ij}^-(S_i^x S_j^y - S_i^y S_j^x) + q_{ij} S_i^z S_j^z] \quad (\text{S18})$$

$$+ g_{ij}^-(S_i^x S_j^x - S_i^y S_j^y) + h_{ij}^+(S_i^x S_j^y + S_i^y S_j^x)]. \quad (\text{S19})$$

Here, g^+ and h^- terms correspond to “flip-flop” type transitions, exchanging one unit of spin polarization,

$$(S_i^x S_j^x + S_i^y S_j^y) = |+\rangle\langle 0+| + |+-\rangle\langle 00| + |00\rangle\langle -+| + |0-\rangle\langle -0| + h.c. \quad (\text{S20})$$

$$(S_i^x S_j^y - S_i^y S_j^x) = i(|+\rangle\langle 0+| + |+-\rangle\langle 00| + |00\rangle\langle -+| + |0-\rangle\langle -0|) + h.c. \quad (\text{S21})$$

In addition, owing to the strong anharmonic level structure, we may also ignore flip-flop transitions between levels with large energy differences, e.g. terms such as $|+-\rangle\langle 00|$. Finally, we ignore the terms in Eq. (S19) as they correspond to double flip-up or flip-down and rapidly oscillate in time. After these approximations, the effective interaction becomes

$$\bar{H}_{ij}^{dd} \approx -J_0/r^3 [(g_{ij}^+ + i h_{ij}^-) |+\rangle\langle 0+| + |0-\rangle\langle -0| + h.c. + q_{ij} S_i^z S_j^z]. \quad (\text{S22})$$

Now we divide into two cases depending on whether spins i and j belong to the same group or to different groups. In the former case, the quantization axes coincide, and we can simplify $h_{ij}^- = 0$, $g_{ij}^+ = \frac{1}{2}(1 - 3 \cos^2 \theta)$, and $q_{ij} = -(1 - 3 \cos^2 \theta)$ with $\cos \theta \equiv \hat{z} \cdot \hat{r}$. In the latter case, the flip-flop terms are again rapidly oscillating, and only the Ising interaction $S_i^z S_j^z$ remains, resulting in

$$\bar{H}_{ij}^{dd} \approx \begin{cases} -\frac{J_0 q_{ij}}{r^3} \left(-\frac{|+\rangle\langle 0+| + |0-\rangle\langle -0| + h.c.}{2} + S_i^z S_j^z \right) & \text{same group} \\ -\frac{J_0 q_{ij}}{r^3} S_i^z S_j^z & \text{different groups} \end{cases}. \quad (\text{S23})$$

These interactions as well as the single particle terms conserve the total population of spins in $|+\rangle$. Therefore, once the system is initialized into a state with no population in $|+\rangle$, the dynamics remains in the manifold spanned by $|-\rangle$ and $|0\rangle$. Projecting $\sum_i \bar{H}_i + \sum_{ij} \bar{H}_{ij}^{dd}$ into

this manifold, we obtain the Hamiltonian for an effective two-level system. Introducing spin-1/2 operators $\vec{\sigma}$ for two levels $|-\rangle$ and $|0\rangle$, we obtain $H_T = H_A + H_B + H_{AB}$, where

$$H_{A(B)} = \sum_{i \in A(B)} [(\delta_{0,i} - \delta_{B,i})\sigma_i^z + \Omega_{A(B)}\sigma_i^x] + \sum_{i,j \in A(B)} \frac{J_0 q_{ij}}{r_{ij}^3} (\sigma_i^x \sigma_j^x + \sigma_i^y \sigma_j^y - \sigma_i^z \sigma_j^z), \quad (\text{S24})$$

$$H_{AB} = - \sum_{i \in A, j \in B} \frac{J_0 q_{ij}}{r_{ij}^3} \sigma_i^{z_A} \sigma_j^{z_B}, \quad (\text{S25})$$

up to a constant.

Finally, we remark one particularly interesting aspect of this Hamiltonian in the dressed-state basis, i.e., quantization along σ_i^x . With sufficiently strong driving, σ_i^x becomes a good spin polarization basis, and one can rewrite the interactions in terms of $\sigma^\pm = \sigma^y \pm i\sigma^z$, wherein the intra-group interaction becomes $\propto \sigma_i^x \sigma_j^x + (\sigma_i^+ \sigma_j^+ + \sigma_i^- \sigma_j^-)/2$ and the inter-group interaction $\propto (\sigma_i^+ \sigma_j^- + \sigma_i^- \sigma_j^+ + h.c.)$. Here, we find that spin exchange terms ($\sigma_i^+ \sigma_j^- + h.c.$) are missing in the intra-group interaction. Omitting the energy non-conserving terms such as $\sigma_i^+ \sigma_j^+$ (secular approximation with a strong driving strength Ω), we obtain the effective Hamiltonian described in the main text.

4 Resonance Counting Theory

In this section, we provide a detailed study of the single particle resonance counting theory. We will first focus on the case of quenched on-site potential disorder, deriving the disorder-dependent power-law relaxation presented in the main text. Then, we generalize the result to the case when disordered potentials are time-dependent.

4.1 Disorder-dependent Power-law Decay

As discussed in the main text, we estimate the survival probability of a single spin excitation based on a simple counting argument. At time t , we compute the probability $\text{Pr}(k; t)$ that the central spin is connected to $k - 1$ other spins via a network of resonances, as defined in the

main text. Assuming that the population of the excitation is equally shared among a resonating cluster, the survival probability is given as

$$P(t) \approx \sum_{k=1}^{\infty} \frac{1}{k} \Pr(k; t). \quad (\text{S26})$$

reducing our problem to the computation of $\Pr(k; t)$. Below we will show that the dominant contributions arise from $k = 1$, suggesting that finding a single resonant partner is usually enough to delocalize the spin excitation over the entire sample.

In general, the exact calculation of $\Pr(k; t)$ is difficult. This is because the connectivity of the resonance network is correlated due to the spatial structure (d -dimensional Euclidean space) as well as a given assignment of random on-site potentials, e.g., if spin pairs (a, b) and (b, c) are pair-wise resonant, it is likely that the pair (a, c) is also resonant, etc. However, the qualitative behavior of $\Pr(k; t)$ can still be well-understood by ignoring these correlations. In such a case, we may assume that the number of resonant partners ℓ for a spins is drawn from a probability distribution $p(\ell)$ and that this process can be iterated for each partner. We note that such a process may not terminate, in which case the central excitation becomes delocalized over a macroscopic number of spins. We first compute $p(\ell)$ as a function of time t . For $\ell = 0$, a spin of interest (spin- i) must not have any resonating spins at any distance from r_{\min} to $R(t) \equiv (J_0 t)^{1/3}$, where r_{\min} is the short-distance cut-off. Hence, $p(0; t)$ is given as a product of probabilities:

$$p(0; t) = \prod_{r_{\min} \leq r < R(t)} \left(1 - 4\pi n r^2 dr \frac{\beta J_0 / r^3}{W_{\text{eff}}} \right) \quad (\text{S27})$$

$$= \exp \left[- \int_{r_{\min}}^{R(t)} \frac{4\pi Q_{\text{res}}}{r} dr \right] \quad (\text{S28})$$

where $4\pi n r^2 dr$ is the probability of finding a spin at distance r , and $Q_{\text{res}} = \beta J_0 / (W_{\text{eff}} r^3)$ is the probability that the spin resonates with the spin- i . Defining $\lambda(t) = 4\pi Q_{\text{res}} (\ln R(t) - \ln r_{\min})$, we obtain $p(0; t) = \exp[-\lambda(t)]$. Similarly, we can calculate $p(\ell; t)$ for $\ell > 0$, and obtain $p(\ell; t) = \frac{1}{\ell!} (\lambda(t))^\ell e^{-\lambda(t)}$, which is the Poisson distribution with mean $\lambda(t)$.

To show that the dominant contribution of Eq. (S26) arises from the $k = 1$ term, we consider the probability of the termination of the resonance finding process, P_{term} . It satisfies the self-consistency equation

$$P_{\text{term}} = e^{-\lambda} + \sum_{\ell=1}^{\infty} \frac{\lambda^{\ell} e^{-\lambda}}{\ell!} (P_{\text{term}})^{\ell}, \quad (\text{S29})$$

where the first term corresponds to the case where the initial spin does not have any resonance up to time t , while the second term implies the termination of each sub-graph generated from ℓ resonant spins. For sufficiently large λ , P_{term} becomes small, and its contribution is dominated by the first term ($\ell = 0$). In our case, $\lambda(t)$ is a function of time which diverges in the limit $t \rightarrow \infty$. As we are interested in the late time dynamics, we may consider the first term only. In terms of $\text{Pr}(k; t)$, this corresponds to approximating $\text{Pr}(k; t) \sim 0$ for $k > 2$. Finally, noting that that $\text{Pr}(k = 1; t) = p(0; t)$, we recover the expression in the main text.

4.2 Time-dependent Disorder

Now we consider the case of time-dependent disorder. For concreteness, we assume that the on-site potential disorder is given as a sum of a static and a dynamical disorder potential, $\tilde{\delta}_i(t) = \tilde{\delta}_i^s + \tilde{\delta}_i^d(t)$, where the static part $\tilde{\delta}_i^s$ (dynamical part $\tilde{\delta}_i^d(t)$) is random with zero mean and standard deviation W_s (W_d). While $\tilde{\delta}_i^s$ is time-independent, the dynamical component $\tilde{\delta}_i^d(t)$ changes over time by uncorrelated jumps at a rate Γ .⁵ Here, we focus on an experimentally relevant regime where $W_s > W_d \gtrsim nJ_0 \gg \Gamma$.

As already mentioned in the main text, we modify the resonance criteria as follows. Two spins at sites i and j are on resonance at time t if: (1) *at any point in time $t' < t$* , their energy mismatch is smaller than their dipolar interaction strength, $|\tilde{\delta}_i(t') - \tilde{\delta}_j(t')| < \beta J_{ij}/r_{ij}^3$, and (2) the interaction occurs within the time-scale t , $J_{ij}/r_{ij}^3 > 1/t$. While the second part of the condition is unchanged, the first part now captures that a pair may be brought into resonance by spectral jumps. Under the hierarchy of $W_s > W_d \gtrsim nJ_0 \gg \Gamma$, the condition (1) can

be approximated by two independent events: (a) the static energy mismatch is small enough, $|\tilde{\delta}_i^s - \tilde{\delta}_j^s| < W_d$, and (b) the dynamical energy mismatch is smaller than the coupling strength, $|\tilde{\delta}_i^d(t') - \tilde{\delta}_j^d(t')| < \beta J_{ij}/r_{ij}^3$ at some time $t' < t$. In combination, the condition (1) is satisfied with the probability

$$P_{\text{res}}(r, t) \approx \frac{W_d}{W_s} \left(1 - e^{-\frac{\beta J_0/r^3}{W_d} \Gamma t} \left(1 - \frac{\beta J_0/r^3}{W_d} \right) \right)$$

which is the product of probabilities for conditions (a) and (b). For the second factor, we used the probability that the initial configuration is off-resonant, $(1 - \frac{\beta J_0/r^3}{W_d})$, and the probability that none of subsequent spectral jumps brings them into resonance $e^{-\frac{\beta J_0/r^3}{W_d} \Gamma t}$. We note that, in practice, one should use $\max(0, 1 - \beta J_0/r^3/W_d)$ instead of $(1 - \beta J_0/r^3/W_d)$ since a probability cannot be less than zero. Finally, the survival probability is obtained by requiring no resonance at every distance r up to $R(t) = (J_0 t)^{1/3}$

$$\overline{P(t)} = \exp \left[- \int_{r=r_0}^{R(t)} 4\pi n r^2 P_{\text{res}}(r, t) dr \right], \quad (\text{S30})$$

where r_0 is the short distance cut-off of the NV separations. We use the cut-off distance $r_0 \sim 1.4$ nm, at which the corresponding dipole-dipole interaction is $J_0/r_0^3 \sim (2\pi) 20$ MHz. Due to dipole blockade, a pair of NV centers closer than r_0 cannot be addressed by microwave driving of Rabi frequency $\Omega \sim (2\pi) 20$ MHz, which we use for initial preparations of spin states. Those spins do not participate in the spin exchange dynamics due to large energy mismatch. We note that, $\lim_{\Gamma \rightarrow 0} P_{\text{res}}(r, t) \rightarrow Q_{\text{res}}(r) = \beta J_0/(W_s r^3)$ and the Eq. (S30) correctly reduces to the disorder-dependent power-law decay.

5 Detailed Analysis of Thermalization Experiments

5.1 Effects of Incoherent Dynamics

In our Hartman-Hahn experiments, the spin dynamics are governed by both coherent cross-relaxation and incoherent depolarization. These two effects have qualitatively different depen-

dence on the driving strength and can be clearly distinguished in our observations. To perform a detailed analysis of the results presented in the main text, we focus on the coherent dynamics by normalizing our data at the Hartman-Hahn resonance $\Omega_A = \Omega_B$ via a sufficiently detuned case $|\Omega_A - \Omega_B| \gg nJ_0$, at which the spin relaxations are dominated by incoherent dynamics (Fig. S7, blue line). Such normalization can be justified only if the two effects are independent and multiplicative. This is the case if the incoherent dynamics are induced by an independent Markovian noise, which results in an exponential and multiplicative factor $e^{-\gamma t}$. In our experiment, however, we observe a stretched exponential $e^{-\sqrt{t/T}}$ decay profile from incoherent dynamics (Fig. 2D in the main text). Below, we explain why such incoherent decays are still factorizable.

Our incoherent dynamics can be modeled as follows. (See Ref. (2) for more details). Each spin at site i undergoes incoherent depolarization at rate γ_i . This rate γ_i is determined by the microscopic local environment of the spin and follows a random distribution $\rho(\gamma; T_1^\rho)$, such that the ensemble averaged polarization decays as a stretched exponential

$$e^{-\sqrt{t/T_1^\rho}} = \int_0^\infty \rho(\gamma; T_1^\rho) e^{-\gamma t} d\gamma. \quad (\text{S31})$$

The analytical expression as well as the microscopic origin of the distribution $\rho(\gamma; T_1^\rho)$ are presented in Ref. (2). At the Hartman-Hahn condition, both the incoherent process and the coherent cross-relaxation lead to depolarization (see Fig. S7). Hence, at time t , the rate of depolarization for spin- i is given by $\dot{p}_i(t) = -[\gamma_i + f_i(t)]p_i(t)$, where $f_i(t)$ is the rate of cross-relaxation (which generally depends on the state of other spins). This cross-relaxation, once averaged over an ensemble, leads to a power-law decay as derived in the previous section. The differential equation for the polarization is exactly solvable with the solution $p_i(t) = e^{-\gamma_i t} e^{\int_0^t f_i(t') dt'}$, where one finds a multiplicative exponential factor $e^{-\gamma_i t}$. Crucially, this effect is still factorizable, even

after ensemble averaging:

$$\langle p_i(t) \rangle_{\text{ensemble}} = \int_0^\infty \rho(\gamma; T_1^\rho) e^{-\gamma_i t} d\gamma \left\langle e^{\int_0^t f_i(t') dt'} \right\rangle_{\text{ensemble}} \propto e^{-\sqrt{t/T_1^\rho}} \cdot t^{-\eta}, \quad (\text{S32})$$

where η is the disorder dependent exponent derived in the main text. Physically, this factorization arises because the microscopic environment for each spin, which determines coherent as well as incoherent dynamics, is random and independent. For this reason, in the experiment, we normalize the polarization decay at the Hartmann-Hahn resonance (Fig. S7, red line) by the incoherent decay at the far-detuned case (Fig. S7, blue line).

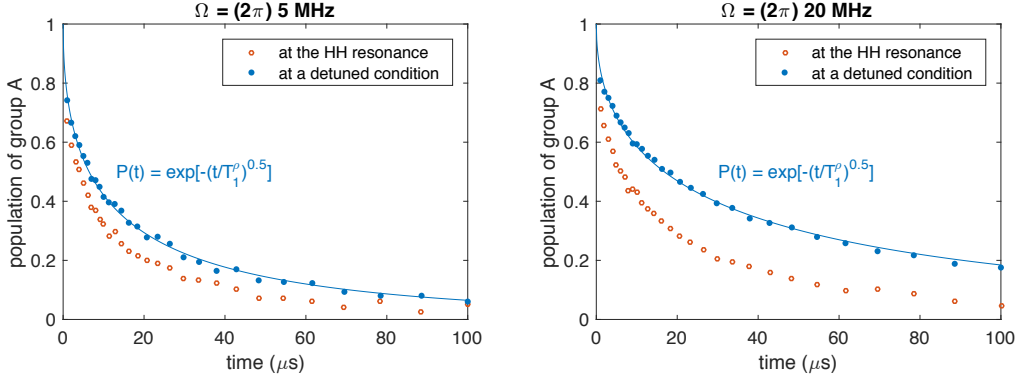


Figure S7: **Unnormalized experimental Data.** Two data sets with different common Rabi frequencies of $\Omega = (2\pi)$ [5, 20] MHz are presented at the Hartmann-Hahn resonance (red) and at the far-detuned case (blue). For the detuned signal, a stretched exponential of power 0.5 is fitted to the data.

5.2 Comparison with Theory

In Fig. S8A, the theory prediction from Eq. (S30) is compared with experimental data for various Rabi frequencies. Based on Monte-Carlo simulations, we extract the parameters W_d and $\tau_d = 1/\Gamma$. We note that we used theory-predicted values for W_s incorporating the saturation seen for $\Omega > (2\pi)$ 15 MHz due to Ising interactions (Fig. S8B inset). As depicted in Fig. S8B, the estimated W_d remains constant ($W_d \sim (2\pi)$ 99 kHz) with increasing driving strength when

$\Omega > (2\pi) 15$ MHz. Since the mean-field interaction cannot be suppressed by strong driving, this result indicates that mean-field fluctuations play an important role for time-dependent disorder. Furthermore, the extracted spectral diffusion time τ_d is consistent with the observed depolarization timescale, including contributions from both coherent cross-relaxation and incoherent spin depolarization.

5.3 Dependence of Spin Cross-relaxation on Initial Spin States

At the Hartmann-Hahn matching condition, relaxation occurs due to spin polarization exchange between group A and B. In principle, this cross-relaxation should not occur if spins in both groups are initially polarized in the same orientation. In Fig. S9, we experimentally measure the polarization in such a case (aligned), compared to the oppositely polarized case (anti-aligned). While the decay of the aligned case is substantially slower than the anti-aligned case for short times, they both decay significantly at late time. This decay at late time can be explained as a consequence of incoherent dynamics; spins in one group may undergo slow, incoherent depolarization due to coupling to the environment, which in turn allows polarization exchange with the other group. To leading order, this effect can be captured by a careful modification to Eq. (S30); we replace the density of spins n with the density of oppositely polarized spins at time t , $n(t) = n_B[1 - e^{-\sqrt{t/T_{1,B}^\rho}}]$, where n_B is the total spin density of group B and $T_{1,B}^\rho$ is the incoherent depolarization time of group B. We note that the corresponding effect for the anti-aligned case is negligible in the limit of $nJ_0 > 1/T_1^\rho$. With this simple correction, our theory model of time-dependent disorder precisely describes the decay behavior of group A even with the aligned initial state (Fig. S9, red line). In this case, the polarization decay of group A significantly accelerates around time $t \sim T_1^\rho = 35\mu s$ at $\Omega = (2\pi) 20$ MHz.

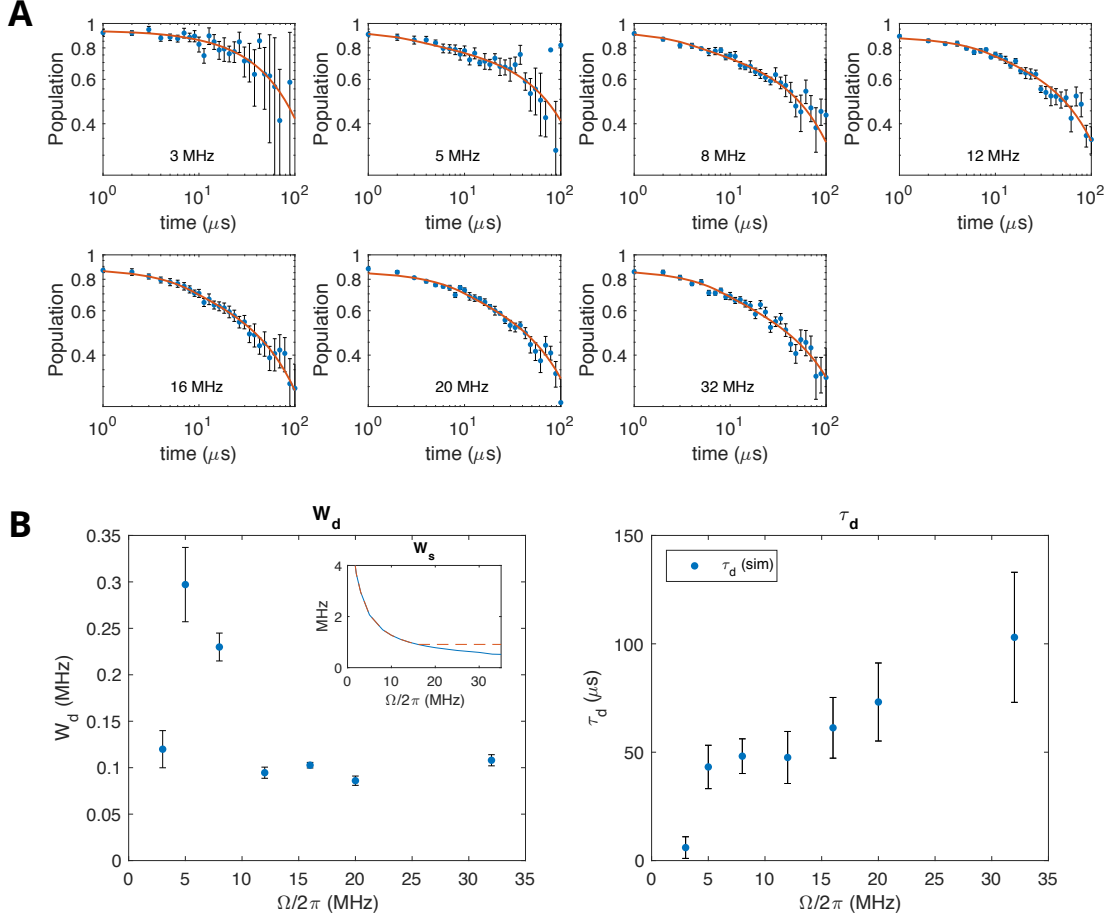


Figure S8: NV Polarization Decay under Hartmann-Hahn conditions. **(A)** Solid lines (red) are Monte-Carlo (MC) fits based upon the time-dependent disorder model with extracted fit parameters from the MC optimization. **(B)** The extracted dynamical disorder W_d (left) and the spectral diffusion time τ_d (right) as a function of Rabi frequency. For comparison, the static disorder W_s is estimated and plotted in the inset, with (dashed red) and without (solid blue) the saturation effect due to Ising interactions. All errorbars are evaluated from the Monte-Carlo fit criterion by which the goodness of fit deviates from a global minimum point by 10%.

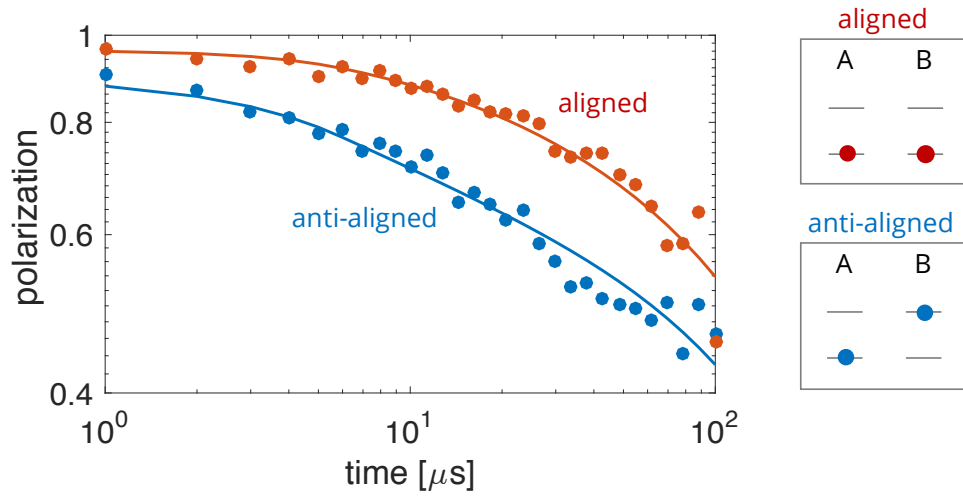


Figure S9: **Spin cross-relaxation at Hartmann-Hahn conditions with different initial states** Depending on initial spin orientations of group A and B, the spin cross-relaxation exhibits different behaviors. Solid lines are theoretical fits to aligned (red) and anti-aligned (blue) cases based upon the time-dependent disorder model. The common Rabi frequency used here is $\Omega = (2\pi) 20$ MHz.

References

1. M. J. Burek, *et al.*, *Nano letters* **12**, 6084 (2012).
2. S. Choi, *et al.*, *arXiv preprint arXiv:1608.05471* (2016).
3. E. Van Oort, M. Glasbeek, *Chemical Physics Letters* **168**, 529 (1990).